Available online at www.sciencedirect.com
ScienceDirect
Trans. Nonferrous Met. Soc. China 35(2025) 4101−4117

Transactions of Nonferrous Metals Society of China
www.tnmsc.cn

Enhancement of ductility and resistance to hydrogen embrittlement in laser powder-bed fusion Ti−6Al−4V alloy by reversible transformation

Huan-qi MA[1], Yu LI[1,2], Wei LI[2], Chun XU[1]

1. School of Materials Science and Engineering, Shanghai Institute of Technology, Shanghai 201408, China;
2. School of Materials Science and Engineering, Shanghai Jiao Tong University, Shanghai 200240, China

Received 20 May 2024; accepted 18 December 2024

Abstract: To simultaneously enhance the strength−plasticity synergy and resistance to hydrogen embrittlement (HE), the post-annealing treatment was conducted in a laser powder-bed fusion Ti−6Al−4V alloy to introduce reversible transformation. The microstructure, mechanical properties, and HE behavior of the alloy were analyzed by electron back-scattered diffraction, transmission electron microscopy, slow-strain-rate tensile test, hydrogen permeation and thermal desorption spectroscopy. The as-printed sample exhibited high strength but limited elongation and high HE sensitivity. When annealed at 550 °C, the elongation was improved but the hydrogen diffusion rate also increased, thus promoting the formation of brittle hydride. When annealed at 750 °C, the reversible transformation $\alpha'\rightarrow\beta\rightarrow\alpha'$ occurred and an $\alpha'/\beta/\alpha'$ sandwich structure formed, thereby enhancing HE resistance (reducing the total elongation loss to 12%) while maintaining high strength (~1116 MPa). The introduction of nanoscale β-phase and soft-oriented α' grain significantly inhibited hydride formation and hydrogen-induced crack propagation.

Key words: Ti−6Al−4V alloy; hydrogen embrittlement; strength−ductility synergy; post-annealing; reversible transformation

1 Introduction

The widely-used α+β Ti−6Al−4V titanium alloys are favored in aerospace, shipbuilding, petrochemicals and biomedicine due to their high specific strength, good fracture toughness, exceptional corrosion resistance and biocompatibility [1]. Despite these advantages, traditional processing methods struggle to meet the increasing demands for high reliability and integrated manufacturing. Additive manufacturing [2], such as laser powder-bed fusion (LPBF) technology, offers a promising solution for fabricating complex configurations of high-melting-point titanium alloys. The ultrafast heating and cooling rates can also promote refined structures with enhanced strength and hardness [3]. However, the LPBF-fabricated Ti−6Al−4V alloys still face challenges, including porosity, elemental segregation, and high internal stress [4], and these negatively impact ductility and restrict their use in structural components.

To address this issue, the strategies to improve the ductility of LPBF-fabricated Ti−6Al−4V focused on: adjusting processing parameters, in-situ alloying, and heat treatment. KHORASANI et al [5] demonstrated that laser processing parameters, such as power and scanning speed, significantly influenced the microstructure and overall mechanical properties. However, the exploration process of optimal parameters was complex and challenging. Moreover, FEREIDUNI et al [6]

Corresponding author: Yu LI, Tel: +86-21-54745420, E-mail: kkkkk@alumni.sjtu.edu.cn;
Wei LI, Tel: +86-21-54745420, E-mail: weilee@sjtu.edu.cn,

https://doi.org/10.1016/S1003-6326(25)66932-9

observed that the addition of B_4C powder led to uniformly-distributed needle-like TiB, thereby preventing the formation of harmful α grain boundaries. Despite these benefits, there remains a lack of deep understanding regarding the compositional homogeneity of mixed powder with varying compositions and particle sizes [7]. In addition to the above strategies, FRKAN et al [8] explored the effects of heat treatment on the microstructure, mechanical properties, and fatigue strength of LPBF-fabricated Ti−6Al−4V specimens, and attributed the enhancement of mechanical properties to the reduction of residual stresses. Nonetheless, most studies only investigated the condition of high temperature annealing above 700 °C, which enhanced ductility at the expense of significant loss in strength, known as the dilemma of strength−ductility trade-off.

Moreover, hydrogen embrittlement (HE), an unpredictable fracture phenomenon caused by residual hydrogen, significantly influences the damage and failure of high-strength titanium alloys. Even a small amount of hydrogen can impair the mechanical properties, leading to loss in ductility and delayed fracture. When hydrogen exceeds its solubility limit, it tends to segregate at the α/β interfaces and forms brittle hydrides [9], such as δ- and ε-hydrides, leading to the reduced plasticity. To solve this problem, various methods have been employed to reduce HE susceptibility. FENG et al [10] highlighted that the grain boundary characteristics play a crucial role in HE resistance. POUND [11] reported that increasing the amount of β-phase through annealing treatment inhibited hydride formation. However, the understanding of HE mechanisms in LPBF-fabricated Ti−6Al−4V alloys remains limited. KACENKA et al [12] observed that LPBF-fabricated Ti−6Al−4V alloys exhibited a higher HE susceptibility compared to wrought alloys.

In this study, the effects of post-annealing treatment on the mechanical properties and HE resistance were investigated in a LPBF-fabricated Ti−6Al−4V bulk alloy. The novelty of this work lay in elucidating the relationship among the complex microstructure evolution, including the precipitation of α-phase and the reverse transformation of β-phase, the strengthening and toughening mechanisms of the LPBF-fabricated Ti alloy. Additionally, the hydrogen trapping abilities of the constituent phases were semi-quantitatively evaluated using scanning Kelvin probe. The hydrogen-related behavior was characterized through hydrogen permeation testing and thermal desorption spectroscopy (TDS). Furthermore, the damage mechanism, the nucleation and propagation of hydrogen-induced-cracks were revealed.

2 Experimental

2.1 Materials and heat treatment

The Ti−6Al−4V powder used for LPBF was produced via high-purity argon atomization, with a particle size range of 25−45 μm. The HBD−150T printer, manufactured by Shanghai Laser & Optical Technology Co., Ltd., China, was operated at a laser power (spot size of 0.1 mm, in Gaussian distribution) of 170 W and a scanning speed of 1 m/s. The substrate was preheated to 100 °C and the printing process involved the *XY* plane as the build plane, with the *Z* axis as the build direction. After LPBF, the printed Ti−6Al−4V samples were annealed in a muffle furnace at 550 and 750 °C for 2 h each, followed air cooling, designated as “550A” and “750A” samples, respectively.

2.2 Slow-strain-rate tensile tests

The mechanical properties and hydrogen embrittlement sensitivity were evaluated through slow-strain-rate tensile (SSRT) testing using dog-bone shaped specimens with a gauge length, width and thickness of 10 mm, 3.2 mm and 1 mm, respectively. Electrochemical hydrogen charging was carried out in a solution comprised 0.2 mol/L H_2SO_4 and 1 g/L CH_4N_2S, with a current density of 10 mA/cm^2 and a charging time of 3 min. Subsequently, the SSRT testing was conducted on a universal testing machine (Zwick BTC-T1-FR020 TN. A50) with an extensometer at a strain rate of 10^{-5} s^{-1}.

2.3 Microstructural characterization

The microstructure morphologies and phase constitutions were characterized using scanning electron microscopy (SEM) and X-ray diffraction (XRD). The samples for SEM examination were etched with Kohler reagent for 10−15 s. XRD tests were conducted with a Japanese Rigaku D/max 2200PC X-ray diffractometer in a 2θ range from 30° to 80° with a scanning rate of 5 (°)/min, using a

Cu K_α radiation source (λ=0.154 nm). The tube voltage and current were set to be 40 kV and 20 mA, respectively. Electron back-scattered diffraction (EBSD Oxford) was employed to determine the phase composition, grain size and dislocation density of the samples. The size and distribution of the precipitated phases were characterized using a JEOL JEM 2100F field emission transmission electron microscope (TEM).

2.4 Hydrogen penetration and TDS tests

Electrochemical hydrogen permeation tests were conducted at room temperature using H-type double electrolyzers. The sample surface was nickel-plated prior to the hydrogen penetration. In a three-electrode system connected to an electrochemical workstation, the tested sample, platinum, and Hg/HgO electrodes were used as working, auxiliary and reference electrodes, respectively. The hydrogen desorption rate was studied using a TDS device (INFICON, USA). The TDS samples were heated from 25 to 825 °C at different rates of 50, 100 and 200 °C/h, respectively, and at a current density of 20 mA/cm^2 for 6 h. The hydrogen desorbed from the sample during the heating process was measured using a quadrupole mass spectrometer.

2.5 Hydrogen-induced cracks and surface potential tests

To observe the hydrogen-induced cracks, flat samples with dimensions of 10 mm × 5 mm × 1 mm were hydrogen charged at a current density of 20 mA/cm^2 for 6 h. Subsequently, the indentation tests were conducted on a ZHR4150 apparatus under a load of 1.5 kN. Atomic force microscope (AFM XE−70) equipped with a scanning Kelvin probe force microscope (SKPFM) was employed to examine the potential distribution in a 2.5 μm × 2.5 μm region at a frequency of 0.2 Hz.

3 Results

3.1 Mechanical properties

Figure 1(a) shows the engineering stress−strain curves of the as-printed (AP), 550A and 750A Ti−6Al−4V samples before and after hydrogen charging. Before hydrogen charging, the AP sample

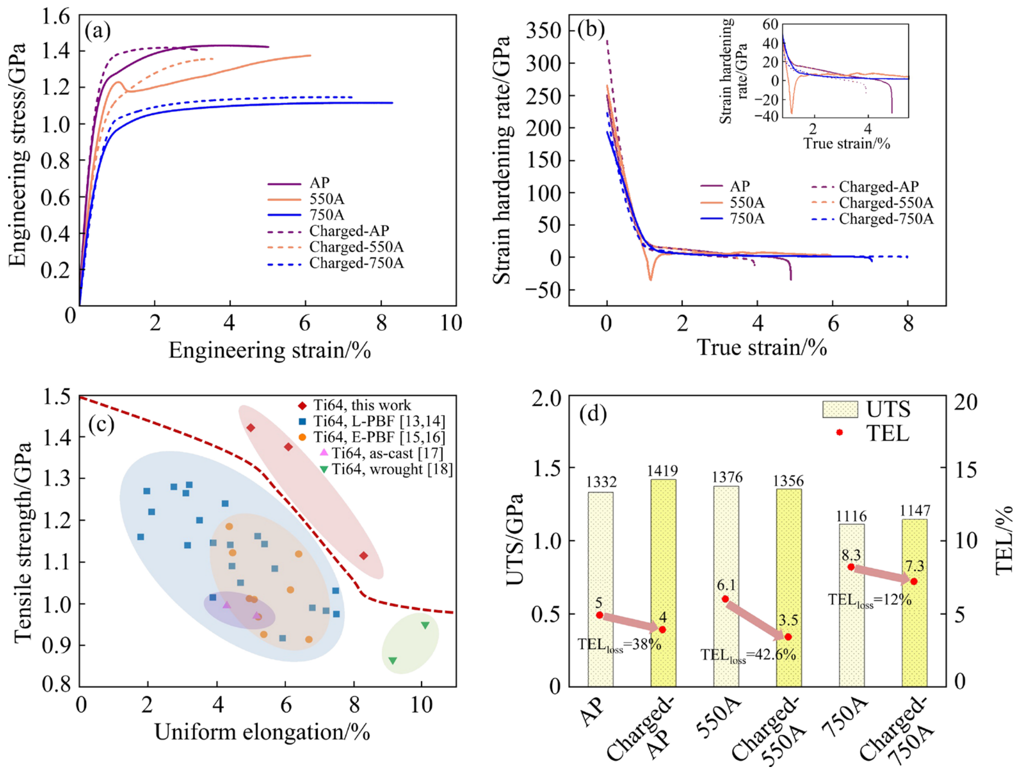

Fig. 1 (a, b) Engineering stress−strain and corresponding strain hardening curves of AP, 550A and 750A samples before and after hydrogen charging; (c) Comparison of tensile properties of studied LPBF-fabricated Ti−6Al−4V alloy with previous works [13−18]; (d) Comparison of strength−ductility synergy and HE resistance (TEL$_{loss}$) of AP, 550A and 750A samples before and after hydrogen charging

exhibited a high ultimate tensile strength (UTS) exceeding 1422 MPa but a limited total elongation (TEL) below 5%. Compared to the AP sample, the 550A sample showed an increase in TEL without compromising yield strength (YS). The 750A sample exhibited the highest TEL (~8.3%) with minimal reduction in UTS. After hydrogen charging, all samples suffered loss in elongation (TEL_{loss}), which was utilized to assess the HE susceptibility. Notably, the 550A and 750A samples exhibited the highest and the lowest elongation losses of 42.6% and 12%, respectively. Detailed data are presented in Table 1. Figure 1(b) displays the corresponding strain hardening curves. Both the 550A and 750A samples exhibited higher strain hardening rates than the AP sample especially at large strains, contributing to the increased ductility. Figure 1(c) compares the tensile properties of the annealed LPBF-fabricated Ti−6Al−4V with previous studies [13−18]. The post-annealing treatment significantly enhances the strength−ductility combination, with the maximum YS exceeding 1286 MPa and the maximum elongation reaching ~8.3%. Figure 1(d) illustrates the mechanical properties and elongation loss values of the AP, 550A and 750A samples before and after hydrogen charging. Results indicate that the 750A sample achieves an optimal balance of strength−ductility and strong resistance to HE.

3.2 Microstructure

Figures 2(a−f) show the SEM images of the AP, 550A and 750A Ti−6Al−4V samples. The AP sample displayed a typical needle-like α'-martensite structure without visible defects. When annealed at 550 °C, the overall morphology of the α'-martensite remained unchanged. However, a high annealing temperature of 750 °C led to a significant microstructure refinement: the primary lath-substructure became less clear, and a small amount of bright β phases were observed at the lath interfaces. To quantitatively characterize the phase constitutions, Figs. 2(g, h) show the XRD patterns of the three Ti−6Al−4V samples. Before hydrogen charging, the AP and 550A samples exhibited fully hexagonal close-packed (hcp) peaks of α or α'-Ti phases. The 750A sample showed weak peaks of β(110) and β(200), consistent with the SEM results. The volume fraction of the β phase was calculated to be ~2.8%. After hydrogen charging, the formation of δ-TiH_2 hydride was detected in both the AP and 550A samples, whereas the peaks of δ-TiH_2 were not observed in the 750A sample.

Figure 3 shows the phase maps and inverse pole figures (IPFs) of the AP, 550A and 750A Ti−6Al−4V samples. The AP sample was characterized by a lath-type α'-martensite matrix with random distributions of grain orientations. The 550A sample exhibited a similar morphology of α'-martensite while the 750A sample displayed a dual-phase structure consisting of β phases distributed along the lath boundaries or at multi-junctions, despite its low volume fraction. The kernel average misorientation (KAM) maps and the distribution of α'-lath thickness are illustrated in Fig. 4. The KAM value represented the distribution of geometrically necessary dislocations (GNDs), which were used to explain the accumulated plasticity in deformed grains [19]. The 750A sample exhibited a significantly lower average KAM value compared to the AP and 550A samples, indicating that extensive dislocation recovery occurred during the high temperature annealing process. Additionally, the average widths of the martensite laths for the AP, 550A and 750A samples were measured to be approximately 0.398, 0.421 and 0.423 μm, respectively. The martensite lath almost remained unchanged thickness after annealing at different temperatures.

Figure 5 shows the TEM images and corresponding selected area electron diffraction (SAED) patterns of the 550A and 750A Ti−6Al−4V samples. The 550A sample exhibited a nano-lath structure of the α'-matrix, and large numbers of

Table 1 Statistical tensile properties of different samples before and after hydrogen charging

Sample	Before hydrogen charging			After hydrogen charging			TEL_{loss}/%
	YS/MPa	UTS/MPa	TEL/%	YS/MPa	UTS/MPa	TEL/%	
AP	1286±20	1422±22	5.0±0.2	1382±21	1419±20	3.1±0.2	38.0
550A	1186±19	1376±18	6.1±0.3	1115±16	1356±18	3.5±0.2	42.6
750A	1009±16	1116±17	8.3±0.4	1020±15	1147±19	7.3±0.3	12.0

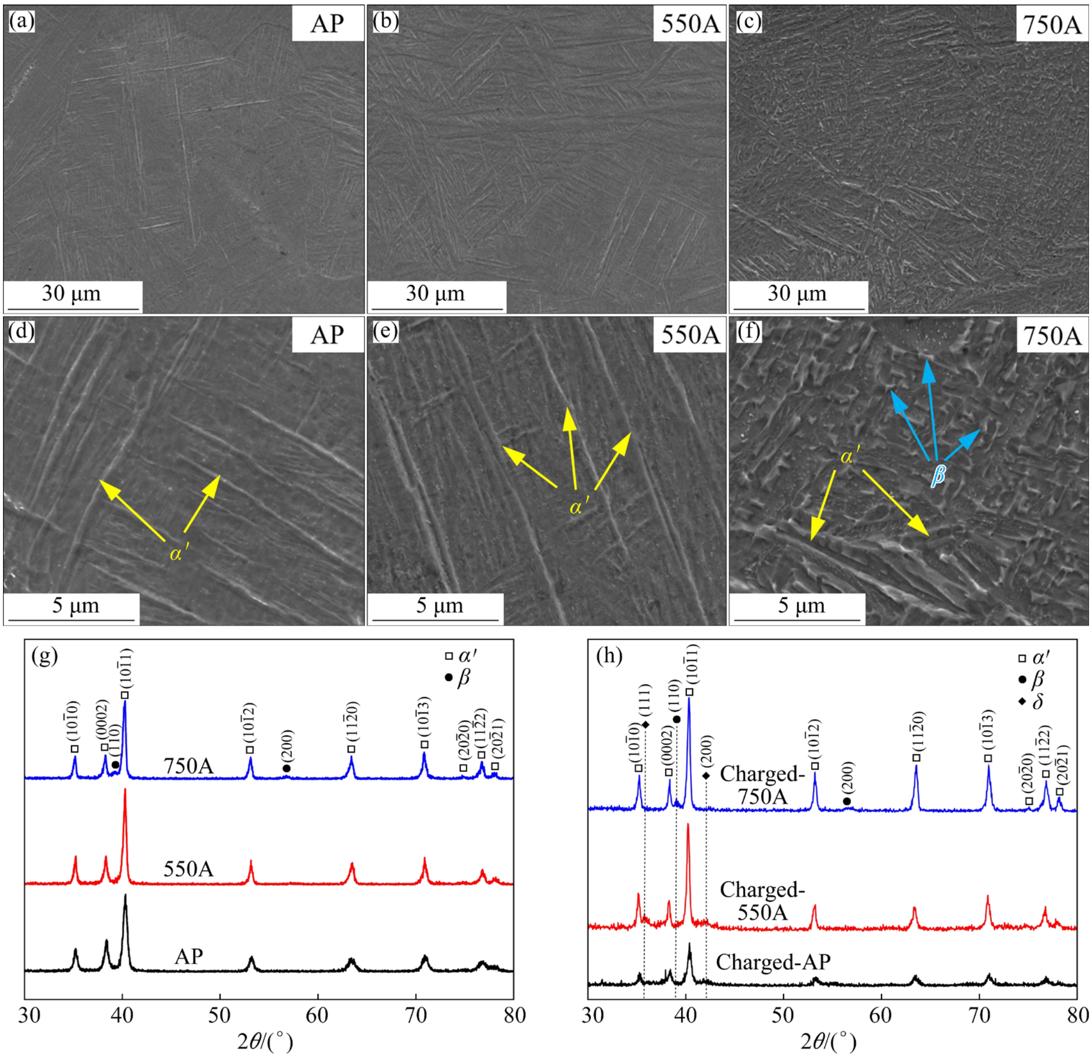

Fig. 2 SEM images of AP (a, d), 550A (b, e) and 750A (c, f), and their XRD patterns before (g) and after (h) hydrogen charging

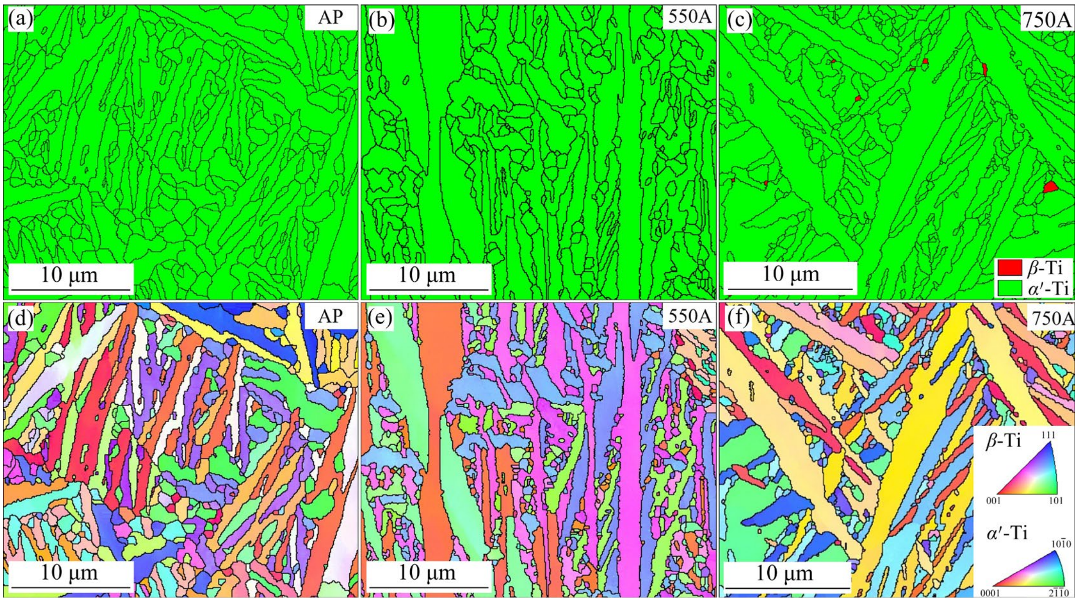

Fig. 3 Phase maps (a, b, c) and IPFs (d, e, f) of AP, 550A and 750A samples

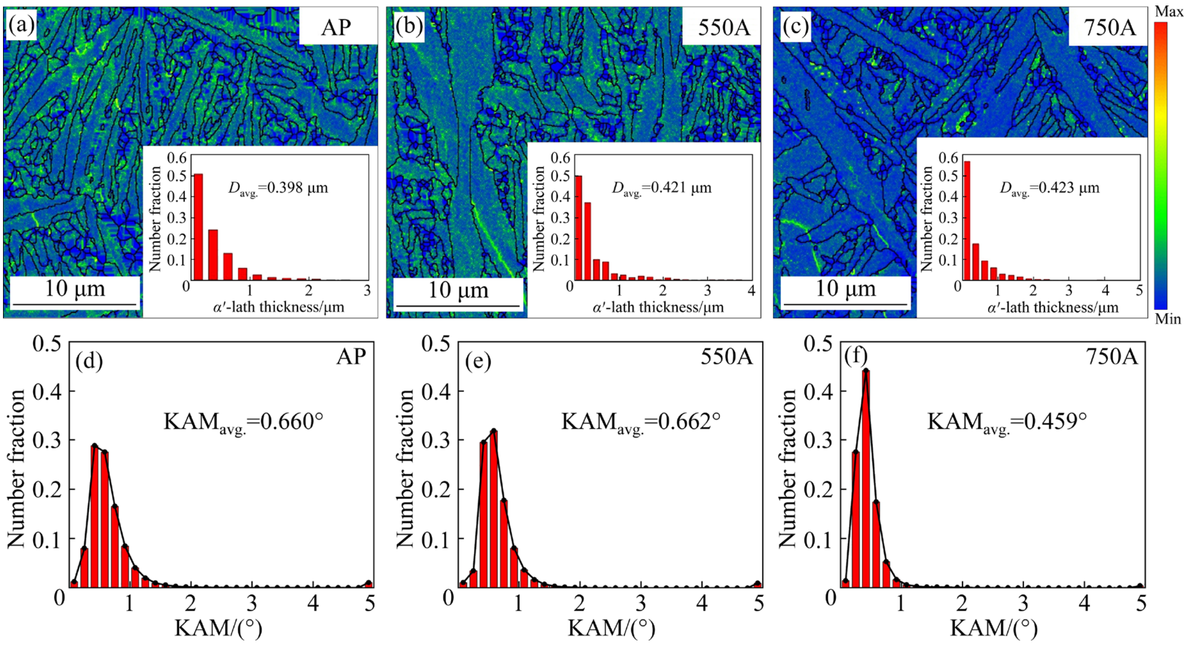

Fig. 4 KAM maps (a, b, c) and distributions of KAM values (d, e, f) of AP, 550A and 750A samples (The insets in (a, b, c) are distributions of α'-lath thickness)

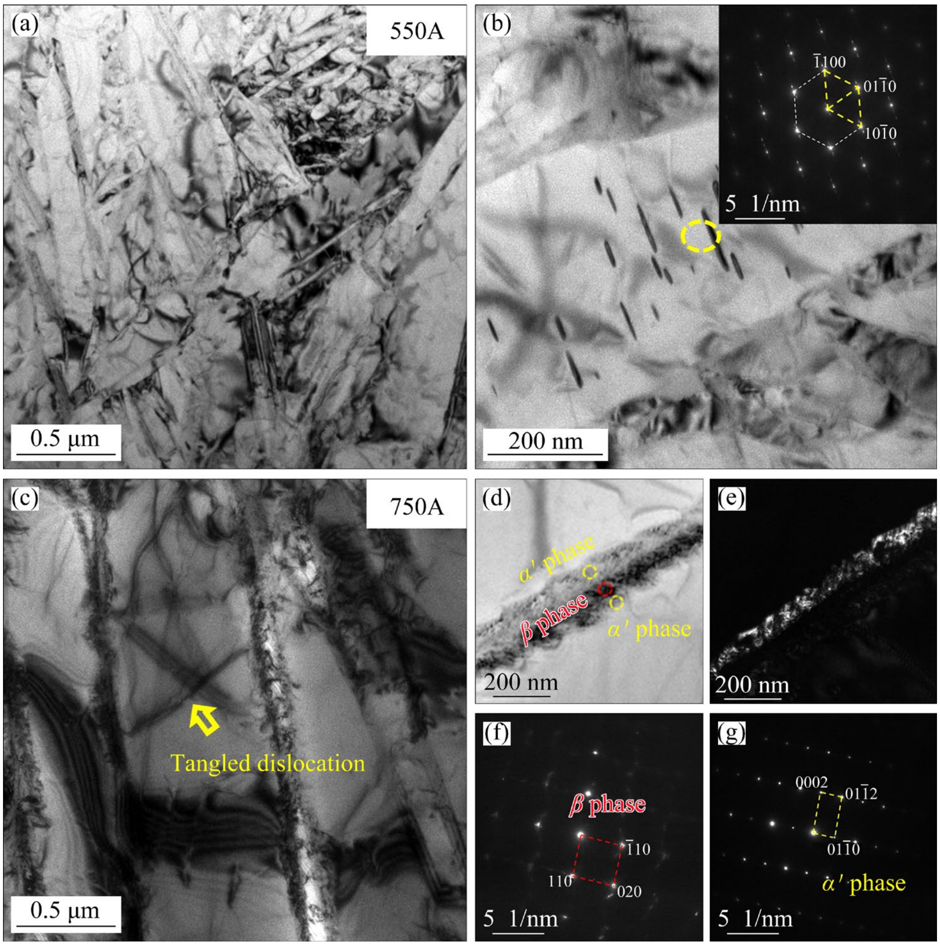

Fig. 5 TEM images of nano-sized α precipitates and sandwich $\alpha'/\beta/\alpha'$ structure, and corresponding SAED patterns of 550A (a, b) and 750A (c, d, e, f, g) samples (Local yellow and red circle zones represent α' and β phases zones, respectively)

needle-like precipitates were observed in the lath interior. The local SAED patters confirmed that these precipitates possessed the same hcp crystal structure as the matrix, identifying them as *α* precipitates. The 750A sample exhibited some tangled dislocations. A distinct sandwich structure comprising the nano-lath *α′*/*β*/*α′* was observed, and the formation of such structure was potentially linked to the reversible *α′*→*β* transformation during the high temperature annealing process.

3.3 Hydrogen permeation and TDS test results

The hydrogen permeation curves of the AP, 550A, and 750A Ti−6Al−4V samples are depicted in Fig. 6. The permeation current significantly increased after ~400 s and eventually stabilized at a steady-state density. According to Fick's law, when hydrogen permeation reached a stable state, the apparent diffusion coefficient D_a was calculated using the equation as follows [20]:

$$D_a = L^2/(6t_L) \tag{1}$$

where L was the thickness of the sample, and t_L was the lag time, which corresponded to the time when $I_t/I_\infty=0.63$ (I_t is the current at time t; I_∞ is the steady-state current). For the AP sample, D_a was close to 1.259×10^{-6} cm²/s. After annealing at 550 °C, D_a increased to 1.954×10^{-6} cm²/s. However, when the annealing temperature increased to 750 °C, D_a significantly decreased to 0.420×10^{-6} cm²/s. Notably, the 750A sample exhibited a lower hydrogen diffusion coefficient compared to the AP and 550A samples.

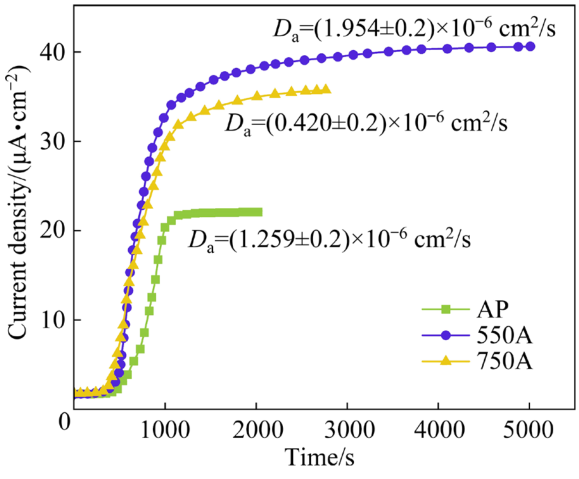

Fig. 6 Hydrogen permeation curves of AP, 550A and 750A samples

Figure 7 shows the TDS results of the AP, 550A and 750A samples at different heating rates. The CHO-Lee method of TDS analysis was used to calculate the capture energy of hydrogen trapping sites [21]. The activation energy E_a for hydrogen atoms to escape from the trapping sites to the sample surface was obtained as follows [21]:

$$\partial\ln(\phi/T_p^2)/\partial(1/T_p) = -E_a/R \tag{2}$$

where ϕ was the heating rate, T_p was the desorption peak temperature, and R was the molar gas constant. As shown in Fig. 7, when the heating rate increased, the position of the hydrogen desorption shifted towards higher temperatures. As calculated, the activation energies E_a of hydrogen atoms in the AP, 550A and 750A samples were 116.6, 86.4 and 168.5 kJ/mol, respectively. The 750A sample exhibited the highest activation energy and the strongest resistance to hydrogen diffusion, which was consistent well with the permeation test results.

4 Discussion

4.1 Effect of post-annealing on microstructure evolution and mechanical properties

As previously illustrated, the ultra-fast melting and cooling process during the LPBF procedure results in the formation of ultra-fine needle-like *α′*-martensite, accompanied by high residual stress, which impedes dislocation motion and makes further plastic deformation difficult. The AP sample exhibits high tensile strength but limited tensile elongation. The post-annealing treatment significantly influences the microstructure evolution and the related mechanical properties. Previous research [22] indicated that the *α* precipitate tended to nucleate within the dislocation substructures of the martensite matrix during annealing. Moreover, the evolution of overall dislocation and GND density is shown in Fig. 8. The GND density is calculated based on the average KAM values obtained above [23], and the average GND density of the 750A sample (3.27×10^{15} m^{-2}) is notably lower than those of the AP (4.58×10^{15} m^{-2}) and 550A (4.61×10^{15} m^{-2}) samples.

Meanwhile, the overall dislocation density (ρ) calculated by XRD spectra shows the same trend. The average dislocation density is calculated by the Williamson−Hall method [24]:

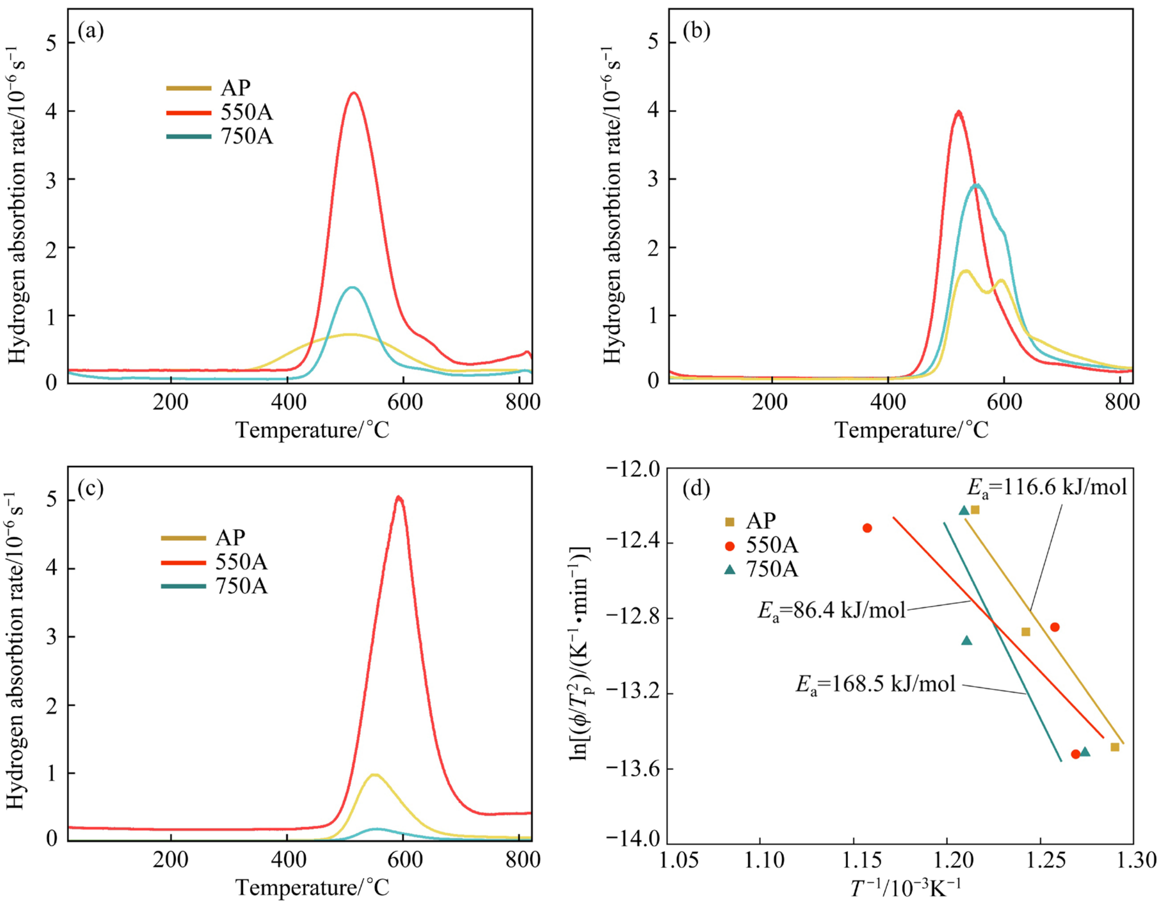

Fig. 7 Hydrogen desorption curves of AP, 550A and 750A samples with different heating rates of 50 °C/h (a), 100 °C/h (b) and 200 °C/h (c); (d) Relationship between $\ln(\phi/T_p^2)$ and $1/T_p$ to calculate activation energy

$$\delta\cos\theta/\lambda=\alpha_1+2\varepsilon\sin\theta/\lambda \tag{3}$$

where δ is the full-width at half of the maximum height, α_1 is a parameter related to the crystalline size, θ, λ and ε are the diffraction angle, X-ray wave-length and strain, respectively. Then, ρ is derived as $\rho=14.4\varepsilon^2/b^2$ [25], where b is the magnitude of Burgers vector. The dislocation density of the 750A sample is 7.29×10^{14} m^{-2}, which is lower than those of the AP (8.03×10^{14} m^{-2}) and 550A (8.31×10^{14} m^{-2}) samples.

During low temperature annealing at 550 °C, atomic and dislocation rearrangements lead to only a slight reduction in dislocation density compared with the AP sample. However, pronounced dislocation recovery occurs at 750 °C, significantly relieving internal stress. Moreover, the α' phase can decompose into $\alpha+\beta$ phases at temperatures above 750 °C [26]. PANTAWANE et al [27] used atomic probe tomography to investigate the decomposition of α'-phase in LBPF-fabricated Ti−6Al−4V alloy, attributing it to the diffusion of V atoms and the formation of V-rich nanoclusters. In this work, a complex reversible phase transformation was observed during high temperature annealing. The β phase nucleated at the lath boundary of the α' martensite during iso-thermal holding, and then partially transformed back into martensite upon cooling, resulting in the formation of a sandwich $\alpha'/\beta/\alpha'$ structure (Fig. 2(f)). Additionally, the distributions of low-angle and high-angle grain boundaries are shown in Fig. 9. The number of low-angle grain boundaries in the 750A sample is significantly larger compared to those of the AP and 550A samples, confirming the presence of such reverse phase transition behavior.

Compared to the AP sample, the 550A sample exhibits a simultaneous rise in both YS and tensile elongation, while the 750A sample demonstrates a notable enhancement in ductility without much loss in strength. The high strength can be explained according to the classic strengthening mechanisms, including solid solution strengthening (σ_0), grain boundary strengthening, precipitation strengthening,

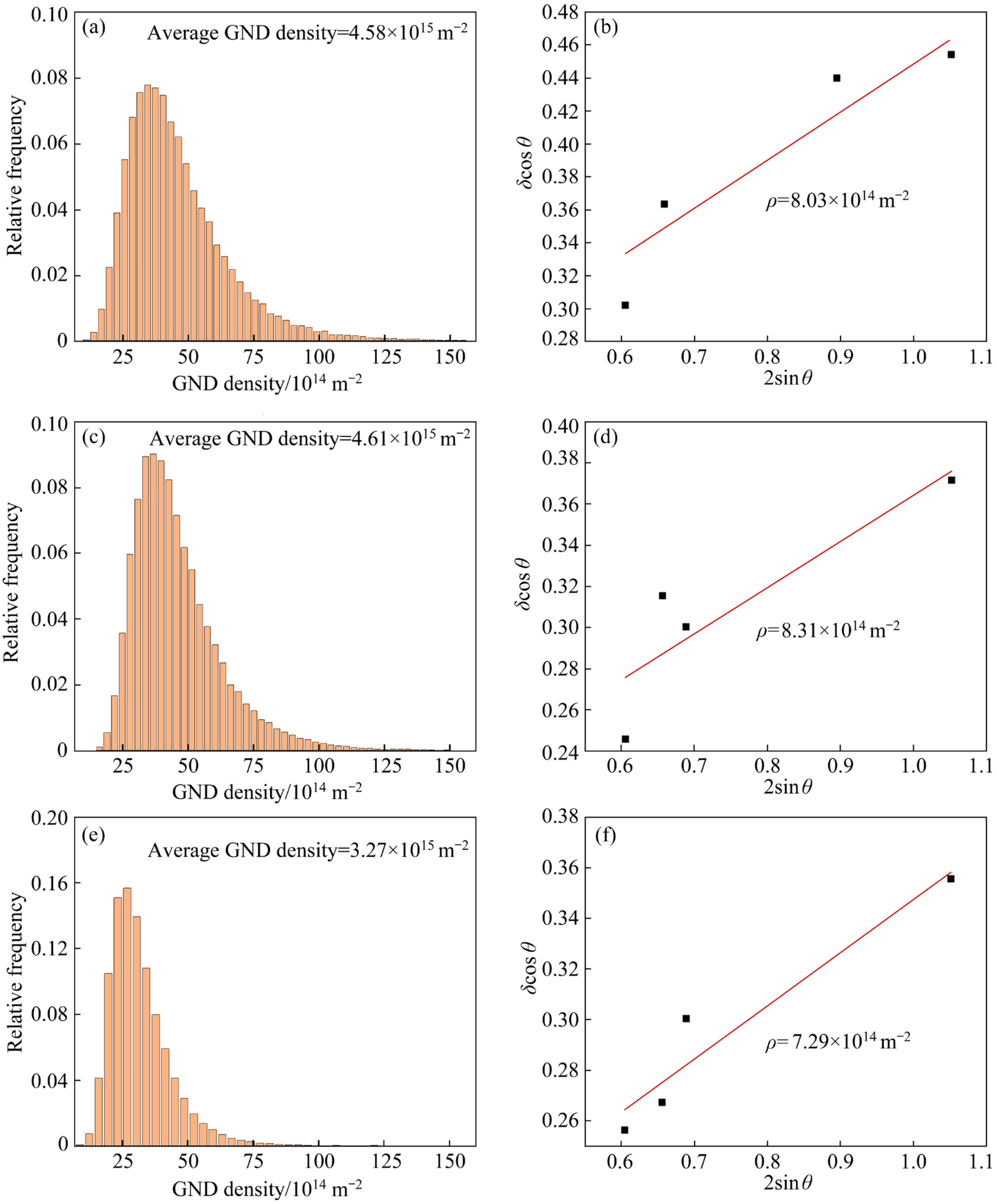

Fig. 8 GND distributions (a, c, e) and overall dislocation densities calculated by Williamson−Hall method (b, d, f) of AP (a, b), 550A (c, d), and 750A (e, f) samples

and dislocation strengthening. Based on previous studies [28], the contributions of α and β phases to the overall yield strength (σ_y) can be calculated using the mixture rule as follows:

$$\sigma_y=f_\alpha\sigma_\alpha+f_\beta\sigma_\beta \tag{4}$$

where σ_α and σ_β are the strength values of α and β phases, respectively; f_α and f_β are their volume fractions.

Dislocation strengthening (σ_ρ) is described by the Taylor model [29]:

$$\sigma_\rho=\alpha M\mu b\sqrt{\rho} \tag{5}$$

where α is a constant that reflects the average strength of dislocation interactions and includes both long-range elastic interactions and short-range reactions between dislocations, and its value is related to the dislocation density. In this work, the α values of α-Ti and β-Ti are estimated to be 0.2 and 0.3, respectively, based on the previous work with a

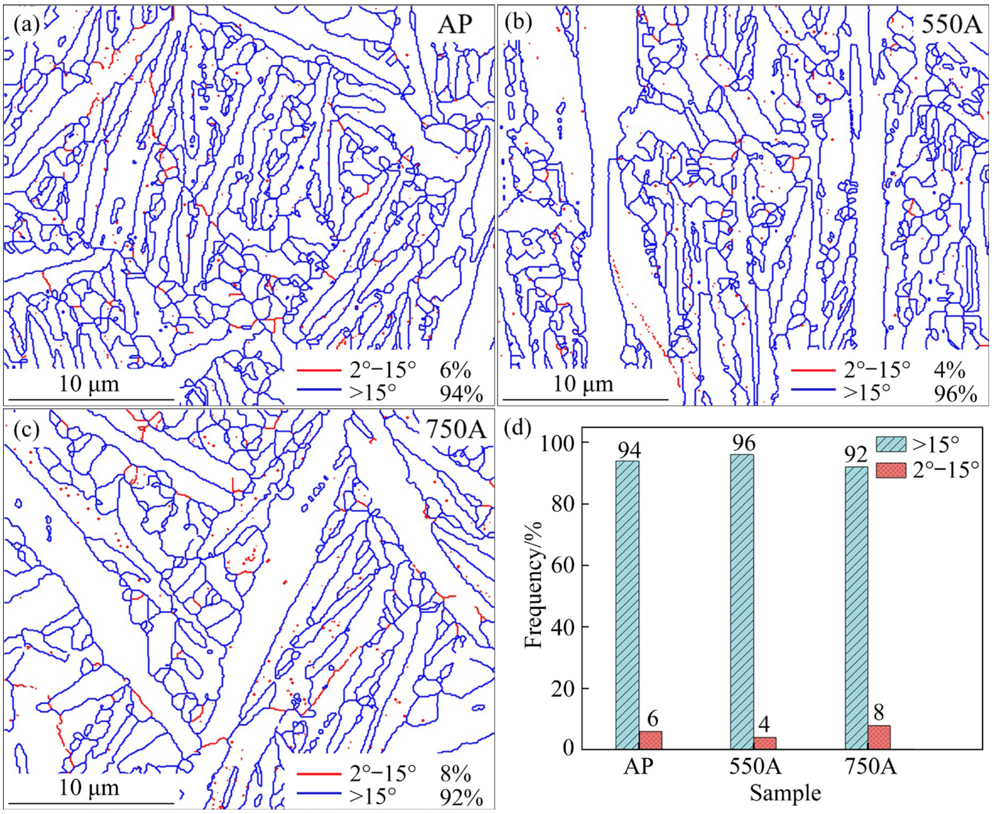

Fig. 9 Distributions of high- and low-angle grain boundaries in AP (a), 550A (b) and 750A (c) samples; (d) Statistics of volume fractions of high- and low-angle grain boundaries in different samples

similar dislocation density of 10^{14} m^{-2} [30]. μ is the shear modulus, M is the Taylor factor, b is the magnitude of the Burgers vector and their values can be referred to previous work of α-Ti and β-Ti alloys [28,31], which are listed in Table 2.

Table 2 Physical constants used for calculating strengthening contributions

Parameter	Description	α-Ti	β-Ti	Source
α	Dislocation interaction constant	0.2	0.3	[30]
M	Taylor factor	1	2.8	[28,31]
μ/GPa	Shear modulus	44	39	[28,31]
b/Å	Burgers vector magnitude	2.95	2.8	[28,31]
K_y/ ($\mathrm{MPa\cdot m^{-1/2}}$)	Hall−Petch constant	0.153	0.5	[28]
K_l/ ($\mathrm{MPa\cdot m^{-1/2}}$)	Hall−Petch constant (PBs)	0.091		This work
L_1/nm	Distance between particles of precipitated phase	34.049		This work

Moreover, grain boundary strengthening (σ_{GB}) can be described by the Hall−Petch relationship in polycrystalline metals [32]:

$$\sigma_{\mathrm{GB}}=K_y d^{-1/2} \tag{6}$$

where d is the grain size and K_y is the strengthening coefficient. The K_y values of α and β phases are estimated to be 0.15 and 0.5 $\mathrm{MPa\cdot \mu m^{-1/2}}$, respectively according to the previous work of duplex TC4 alloy [28]. In the nano-martensitic duplex structure, the strengthening contribution (σ_{PB}) of the α/β boundary can be calculated by the following equation [33]:

$$\sigma_{\mathrm{PB}}=K_l\lambda_l^{-1/2} \tag{7}$$

where λ_l is the measured average thickness of the β-lamellar (λ_l=75 nm) and K_l is the Hall−Petch constant, which is estimated to be 0.091 $\mathrm{MPa\cdot \mu m^{-1/2}}$ according to the number of dislocations crossing the same lamellar.

The formation of the precipitated phases contributes significantly to the precipitation strengthening. According to the Russell−Brown model, the precipitation strengthening σ_{PH} can be expressed as follows [34]:

$$\sigma_{\mathrm{PH}}=0.8\mu b/L_1[1-(E_1/E_2)^2]^{1/2} \tag{8}$$

where L_1 is the distance between precipitated phases; E_1 and E_2 represent the energy per unit length of dislocation lines on two sides of the phase interface when a dislocation traverses it. Detailed physical constants are given in Table 2.

The contributions of individual strengthening mechanisms are summarized in Fig. 10. The calculated YS results align well with the experimental measurements. The high YS of the 550A sample is primarily attributed to high density of α precipitates and highly-dislocated nano-lath α'-martensite. Notably, the 550A sample exhibits an unexpected discontinuous yielding behavior (Fig. 1(b)). YANG et al [35] attributed this elasto-plastic phenomenon to the heterogeneous deformation between the matrix and the intragranular precipitate. Moreover, the low-temperature annealing promotes the rearrangement of lattice defects (such as vacancies and interstitial atoms), leading to an increase in tensile elongation. Compared to the AP sample, the slight decrease in the YS of the 750A sample is related to the reduced Taylor hardening due to significant dislocation recovery. The highest ductility of the 750A sample can be attributed to the following aspects: (1) Residual stress and internal strain within the plate are effectively relieved, promoting the dislocation movement [36] and facilitating plastic deformation; (2) The reversed β phase acts as a soft phase [37], regulating strain partitioning and increasing TEL; (3) The distributions of Schmid factor for basal slip, as depicted in Fig. 11, indicate that the 750A sample has higher Schmid factor, predominantly in the range of 0.35−0.5, compared to the AP and 550A samples. This suggests a prevalence of soft-orientated grains, which can activate multiple slip systems. Briefly, the occurrence of soft-orientated α'-grains due to the bidirectional reversible $\alpha'\rightarrow\beta\rightarrow\alpha'$ transformation significantly enhances homogeneous plastic deformation.

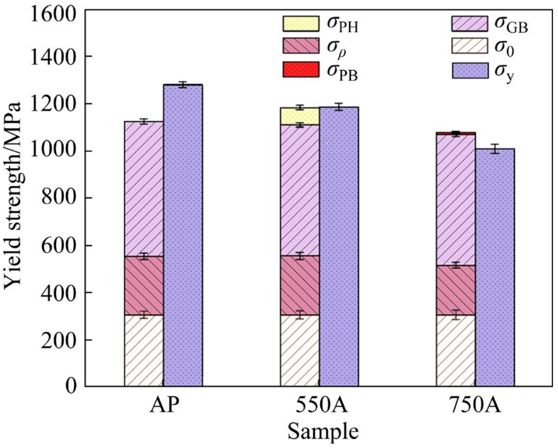

Fig. 10 Comparison of theoretical yield strength and measured yield strength σ_{y} for AP, 550A and 750A samples

4.2 Hydrogen embrittlement mechanisms of complex multiphase microstructure

Compared to the AP and 550A samples, the 750A sample not only exhibits an improved strength−ductility synergy but also demonstrates a lower elongation loss after hydrogen charging, indicating reduced HE susceptibility. Indeed, the HE resistance is closely linked with the nature, quantity, and capacity of hydrogen trapping sites, as well as the hydrogen-related behavior of constituent phases [38].

The three samples show different hydrogen trapping abilities, as indicated by their different activation energies E_{a} (TDS) and apparent hydrogen diffusion coefficients (hydrogen permeation). The 750A sample exhibits the highest activation energy E_{a} and the lowest hydrogen diffusion coefficient, while the 550A sample demonstrates the lowest activation energy E_{a} and the highest hydrogen diffusion coefficient. The hydrogen trapping sites primarily include inclusions, grain boundaries, dislocations and precipitates [39]. Firstly, the 750A sample is characterized by higher amounts of low-angle grain boundaries, which act as effective hydrogen trapping sites due to their high energy barrier for hydrogen diffusion [40]. In contrast, high-angle grain boundaries in the AP and 550A samples serve as channels for hydrogen moving, as they possess high lattice distortion and local stress fields [41]. Secondly, after the ultra-rapid cooling process in LPBF, considerable numbers of dislocation substructures are distributed along the martensite laths. These dislocations not only facilitate hydrogen diffusion but also act as reversible hydrogen traps, promoting the formation of hydrogen gas clusters around them. The movement of these dislocations significantly boosts the hydrogen diffusion coefficient [42]. When dislocation loops encounter grain boundaries, the

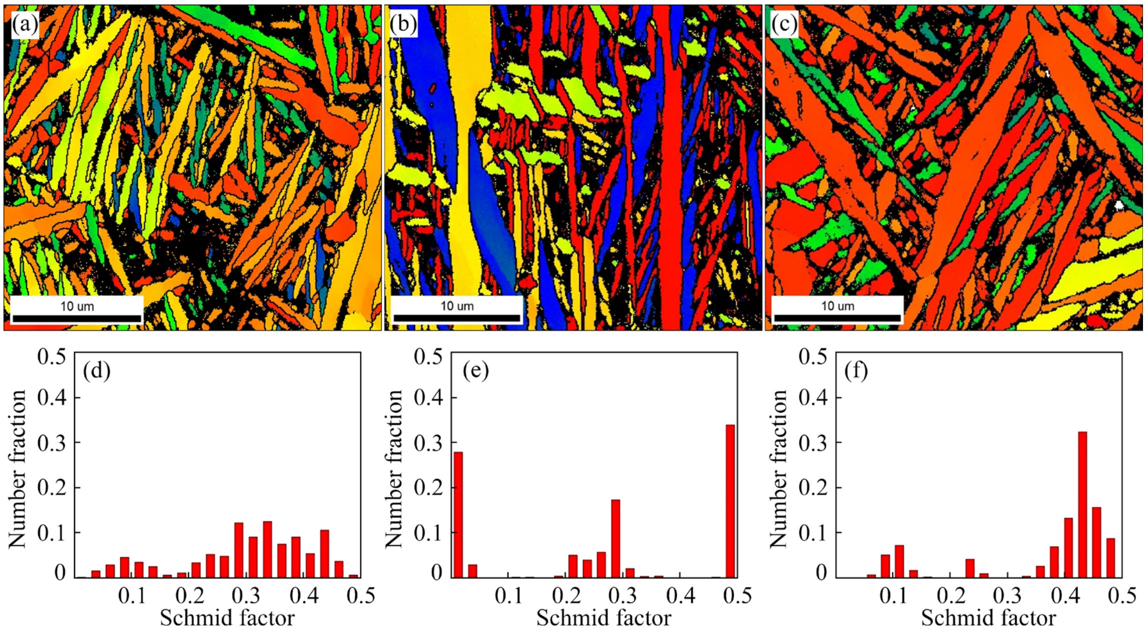

Fig. 11 (a, b, c) EBSD images showing distributions of Schmid factors for $\{0001\}\langle 11\bar{2}0\rangle$ dislocation slip in AP, 550A and 750A samples, respectively; (d, e, f) Statistic results of (a, b, c), respectively

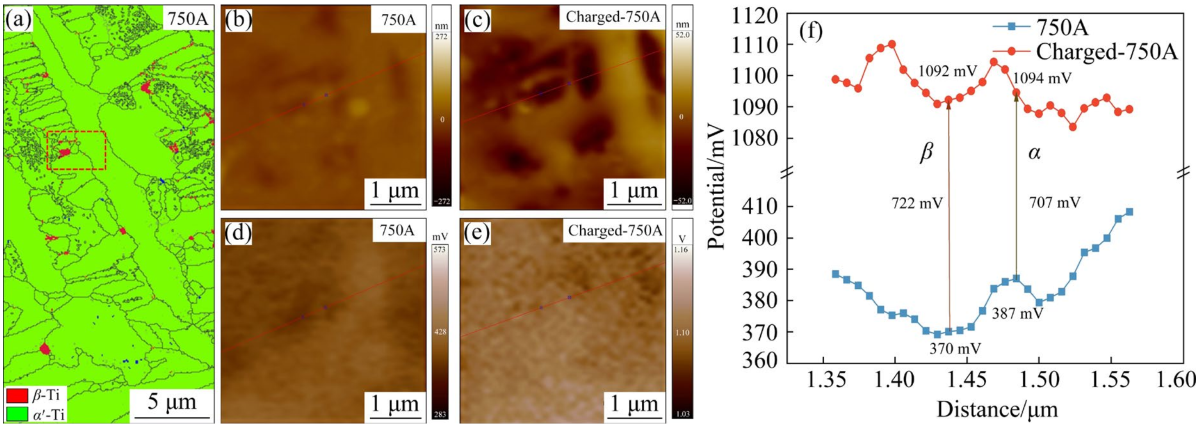

Fig. 12 In-situ EBSD−AFM characterization results of 750A samples before and after hydrogen charging: (a) Phase map; (b, c) AFM morphologies; (d, e) Potential maps; (f) Potential difference of β phase and matrix before and after hydrogen charging

gas clusters release hydrogen atoms into the grain boundaries [43]. Consequently, a high dislocation density promotes hydrogen diffusion. The 750A sample with a lower GND density exhibits a slower hydrogen diffusion rate compared to the AP and 550A samples.

Moreover, the 750A sample contains small amounts of β phase, which has been demonstrated to exhibit strong hydrogen trapping capability [44]. In-situ AFM tests coupled with EBSD techniques were conducted to analyze the surface potential of the constituent phases in the 750A sample, as shown in Fig. 12. After hydrogen charging, the surface potentials of both phases increased. The presence of hydrogen atoms strongly influenced the metal potential or work function. Notably, the surface potential of the β phase increased more significantly than that of the α phase (722 mV vs 707 mV), indicating that the β phase possessed a higher hydrogen trapping ability. Indeed, defects and lattice distortions in the β phase can affect the adsorption and release of hydrogen, thereby promoting hydrogen enrichment or trapping in the β phase [45].

Furthermore, the nucleation and propagation of hydrogen-induced cracks also influence the occurrence of HE [46]. Generally, the mechanisms of HE include hydrogen internal pressure, hydrogen-enhanced decohesion (HEDE), and hydrogen-enhanced local plasticity (HELP) [47]. The HE of α-titanium alloys is closely linked to the formation of titanium hydride, as observed in the 550A sample (Fig. 2(h)). Indentation tests after hydrogen charging indicated that cracks only appeared on the surface of the 550A sample. As shown in Fig. 13, the crack initiated near the δ-TiH$_2$ hydride and propagated along its grain boundaries. SETOYAMA et al [48] observed that the entry of hydrogen into the lattice gap of δ-TiH$_2$ hydride led to lattice expansion. XRD was used to analyze the lattice constants based on the following formula [49]:

$$1/d_{hkl}^2=4(h^2+hk+k^2)/3a^2+l^2/c^2 \tag{9}$$

where h, k and l are Miller indices of diffraction planes; d_{hkl} is the interplanar spacing; a and c represent lattice constants along different axes. The lattice constant after hydrogen charging is significantly larger than that before charging, as depicted in Fig. 14. The larger volume of the hydride relative to the matrix induces a significant distortion, high internal stresses and dislocation piling-ups near the interface during the $\alpha\rightarrow\delta$ transformation, as evidenced by KAM maps (Fig. 13(c)). When these stresses exceed the fracture strength, the samples may undergo a crack incubation period in a hydrogen-rich environment. As the crack propagates along the δ-TiH$_2$ interface, the stress intensity factor at the crack tip gradually increases, ultimately leading to delayed fracture [49]. In contrast, the low average hydrogen content of the 750A sample reduces the driving force for δ-TiH$_2$ formation (Fig. 2(h)). Additionally, the alleviated local stress and finer structure contribute to more homogeneous strain distribution, thus inhibiting the crack formation along the fewer δ-TiH$_2$ interfaces. These observations indicate that the 550A sample exhibits a higher sensitivity to HE compared to the 750A sample.

To conclude, the primary factors leading to HE in the 550A sample are plenty of high-angle grain boundaries and high-density dislocations, which result in lower activation energy for hydrogen diffusion and higher hydrogen diffusion coefficient.

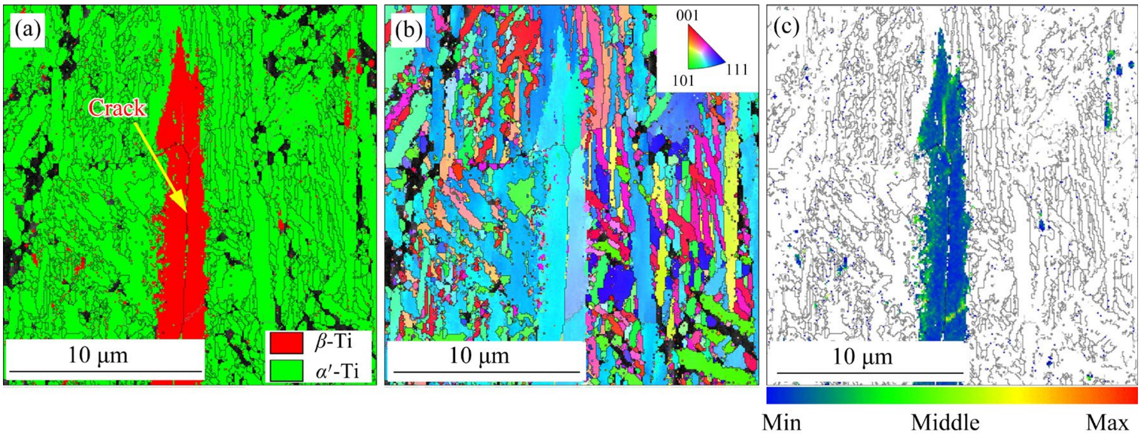

Fig. 13 Phase map (a), IPF image (b) and KAM map (c) of δ-TiH$_2$ in crack tip of 550A sample after hydrogen charging

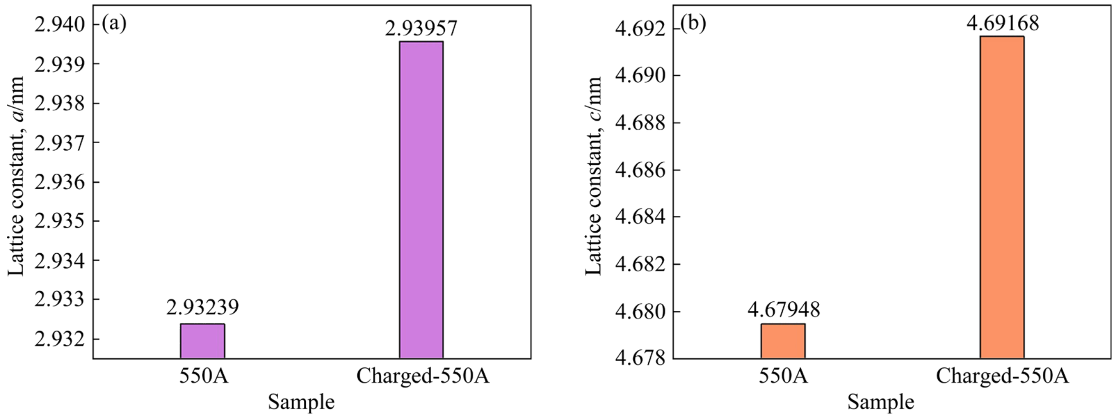

Fig. 14 Changes in lattice constants a (a) and c (b) of 550A sample before and after hydrogen charging

Moreover, the formation of titanium hydrides makes the interface more susceptible to crack nucleation, thereby increasing the sensitivity to HE. Conversely, the 750A sample contains larger amounts of β phase and a higher proportion of low-angle grain boundaries due to the reversible $\alpha'\to\beta\to\alpha'$ transformation, resulting in a higher activation energy for hydrogen diffusion and a lower hydrogen diffusion coefficient. Furthermore, the sandwich structure of $\alpha'/\beta/\alpha'$ also exhibits high resistance to crack nucleation, as the internal soft β phase can absorb the strain energy at the crack tip during propagation. Consequently, the inhibition of titanium hydride formation and reduced stress concentration lead to decreased elongation loss and enhanced resistance to HE.

Figure 15 presents a comparative analysis of the mechanical properties, including strength, ductility, and HE resistance, achieved in this work with those reported in previous studies [12,44,50,51]. NGUYEN et al [51] found that the formation of nanometer/micron-sized voids at grain boundaries activated the intergranular cracking behavior at low hydrogen concentrations. On the contrary, the increase in the volume of the hydride phase at high hydrogen concentrations led to obvious crack initiation and propagation, accompanied with a significant elongation loss of ~38%. KACENKA et al [12] demonstrated that heat treatment reduced the HE sensitivity by 30% in the 3D-printed Ti−6Al−4V sample, but the total elongation was still significantly reduced, which was attributed to the formation of cracks at the hydrides near the α/β interfaces. The post-annealing treatment offers a strategy of simultaneously enhancing the strength−ductility synergy and HE resistance in additive-manufactured alloys. The effectiveness of this treatment is highly dependent on the annealing temperature. An excessively high temperature above the β-transformation may not preserve the nano-lamellar LPBF structure, leading to significant strength loss, whereas a low annealing temperature cannot significantly improve the HE resistance. Therefore, the multi-cycle annealing treatment in a moderate temperature range, inspired by the quenching-lamellar-tempering (QLT) treatment of 9% Ni steel [52], will be the focus of future work to refine the structure unit, enhance the toughness and crack resistance of LPBF-fabricated Ti-alloys through cycle reversible transformation.

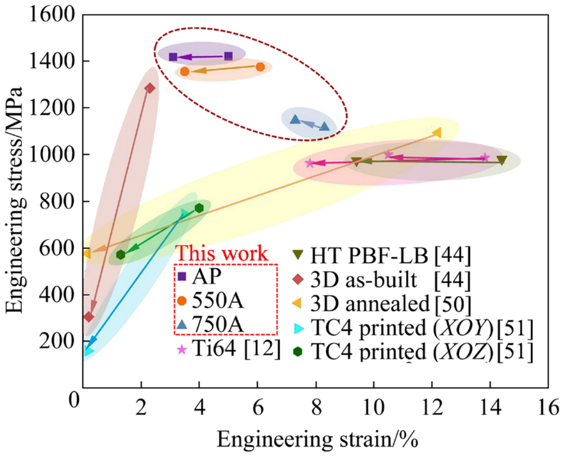

Fig. 15 Comparison of strength, ductility and HE resistance between this work and other Ti−6Al−4V alloys [12,44,50,51]

5 Conclusions

(1) The as-printed Ti−6Al−4V alloy exhibited a fully nano-lamellar α' martensite structure. After annealing at 550 °C, the TEL increases without sacrificing YS. A higher-temperature annealing at 750 °C results in $\alpha'\to\beta$ reverse transformation, thereby forming $\alpha'/\beta/\alpha'$ sandwich structure with abundant dislocation recovery, simultaneously improving TEL (5% vs 8.3%) and HE resistance (TEL_{loss}: 38% vs 12%).

(2) The 550A sample exhibited a higher YS and a larger hydrogen diffusion coefficient compared to the 750A sample. The former was attributed to higher grain boundary strengthening, higher dislocation strengthening and precipitation strengthening. The latter enhanced the formation of brittle titanium hydride, significantly reducing HE resistance.

(3) The highest TEL of the 750A sample originated from the introduced β phases and the soft-oriented α'-grains via bidirectional $\alpha'\to\beta\to\alpha'$ transformation. Its superior HE resistance was attributed to the inhibition of δ-TiH_2 hydride by the β phases, the alleviation of stress concentration, and the impediment of crack propagation by the sandwich $\alpha'/\beta/\alpha'$ structure.

CRediT authorship contribution statement

Huan-qi MA: Methodology, Visualization, Writing − Original draft, Writing − Review & editing; **Yu LI:** Conceptualization, Investigation, Writing − Review & editing, Funding acquisition, Project

administration, Supervision; **Wei LI:** Resources, Writing − Review & editing; **Chun XU:** Supervision, Writing − Review & editing.

Declaration of competing interest

The authors declare that they have no known competing financial interests or personal relationships that could have appeared to influence the work reported in this paper.

Data availability

The data that support the findings of this study are available from the corresponding author upon request.

Acknowledgments

The authors gratefully acknowledge financial support from the National Natural Science Foundation of China (No. 52001213), and the "Chen Guang" Project (No. 20CG65) supported by the Shanghai Municipal Education Commission, China.

References

[1] LIU Shi-shuang, CAI Jian-ming, ZHOU Yi, CAO Jing-xia, ZHANG Wang-feng, DAI Sheng-long, HUANG Xu, CAO Chun-xiao. Influence of annealing temperature on microstructural evolution and tensile behavior of Ti−6Al−4V alloy manufactured by multi-directional forging [J]. Transactions of Nonferrous Metals Society of China, 2024, 34(6): 1864−1877.

[2] GIBSON I, ROSEN D, STUCKER B, KHORASANI M. Additive manufacturing technologies [M]. 3rd ed. Cham, Switzerland: Springer, 2021.

[3] ZHANG Du-yao, QIU Dong, GIBSON M A, ZHENG Yu-feng, FRASER H L, STJOHN D H, EASTON M A. Additive manufacturing of ultrafine-grained high-strength titanium alloys [J]. Nature, 2019, 576(7785): 91−95.

[4] LIU Tian-yu, MIN Xiao-hua, ZHANG Shuang, WANG Cun-shan, DONG Chuang. Microstructures and mechanical properties of Ti−Al−V−Nb alloys with cluster formula manufactured by laser additive manufacturing [J]. Transactions of Nonferrous Metals Society of China, 2021, 31(10): 3012−3023.

[5] KHORASANI A M, GIBSON I, GHADERI A, MOHAMMED M I. Investigation on the effect of heat treatment and process parameters on the tensile behaviour of SLM Ti−6Al−4V parts [J]. The International Journal of Advanced Manufacturing Technology, 2019, 101: 3183−3197.

[6] FEREIDUNI E, GHASEMI A, ELBESTAWI M. Unique opportunities for microstructure engineering via trace B_4C addition to Ti−6Al−4V through laser powder bed fusion process: As-built and heat-treated scenarios [J]. Additive Manufacturing, 2022, 50: 102557.

[7] BRIKA S E, LETENNEUR M, DION C A, BRAILOVSKI V. Influence of particle morphology and size distribution on the powder flowability and laser powder bed fusion manufacturability of Ti−6Al−4V alloy [J]. Additive Manufacturing, 2020, 31: 100929.

[8] FRKAN M, KONECNA R, NICOLETTO G, KUNZ L. Microstructure and fatigue performance of SLM-fabricated Ti6Al4V alloy after different stress-relief heat treatments [J]. Transportation Research Procedia, 2019, 40: 24−29.

[9] DENG Lei, TIAN Zhuang, HAO Yi, WANG Xin-yun, ZHANG Mao, TANG Xue-feng, LI Wen-bin. Effect of hydrogen on hot deformation behavior and microstructure evolution of Ti65 alloy [J]. International Journal of Hydrogen Energy, 2024, 50: 784−795.

[10] FENG Xu-dong, XU You-wei, SHI Yu, GU Yu-feng, KORZHYK V. Effects of microstructure and morphological distribution on hydrogen-embrittlement sensitivity of Ti−6Al−4V alloy welded joint [J]. International Journal of Hydrogen Energy, 2024, 50: 361−371.

[11] POUND B G. The effect of aging on hydrogen trapping in β-titanium alloys [J]. Acta Metallurgica et Materialia, 1994, 42(5): 1551−1559.

[12] KACENKA Z, ROUDNICKA M, EKRT O, VOJTECH D. High susceptibility of 3D-printed Ti−6Al−4V alloy to hydrogen trapping and embrittlement [J]. Materials Letters, 2021, 301: 130334.

[13] BARTOLOMEU F, GASIK M, SILVA F S, MIRANDA G. Mechanical properties of Ti6Al4V fabricated by laser powder bed fusion: A review focused on the processing and microstructural parameters influence on the final properties [J]. Metals, 2022, 12(6): 986.

[14] BUHAIRI M A, FOUDZI F M, JAMHARI F I, SULONG A B, RADZUAN N A M, MUHAMAD N, MOHAMED I F, AZMAN A H, HARUN W S W, AL-FURJAN M S H. Review on volumetric energy density: influence on morphology and mechanical properties of Ti6Al4V manufactured via laser powder bed fusion [J]. Progress in Additive Manufacturing, 2023, 8(2): 265−283.

[15] GHODS S, SCHUR R, SCHLEUSENER R, MONTELIONE A, PAHUJA R, WISDOM C, AROLA D, RAMULU M. Contributions of intra-build design parameters to mechanical properties in electron beam additive manufacturing of Ti6Al4V [J]. Materials Today Communications, 2022, 30: 103190.

[16] NANDWANA P, LEE Y. Influence of scan strategy on porosity and microstructure of Ti−6Al−4V fabricated by electron beam powder bed fusion [J]. Materials Today Communications, 2020, 24: 100962.

[17] LUAN J H, JIAO Z B, LIU W H, LU Z P, ZHAO W X, LIU C T. Compositional and microstructural optimization and mechanical-property enhancement of cast Ti alloys based on Ti−6Al−4V alloy [J]. Materials Science and Engineering: A, 2017, 704: 91−101.

[18] DOLEV O, OSOSKI S, SHIRIZLY A. Ti−6Al−4V hybrid structure mechanical properties—Wrought and additive manufactured powder-bed material [J]. Additive Manufacturing, 2021, 37: 101657.

[19] WANG M M, TASAN C C, PONGE D, RAABE D. Spectral TRIP enables ductile 1.1 GPa martensite [J]. Acta Materialia, 2016, 111: 262−272.

[20] ZHU Xu, ZHANG Ke, LI Wei, JIN Xue-jun. Effect of retained austenite stability and morphology on the hydrogen embrittlement susceptibility in quenching and partitioning treated steels [J]. Materials Science and Engineering: A, 2016, 658: 400−408.

[21] CHOO W Y, LEE J Y. Thermal analysis of trapped hydrogen in pure iron [J]. Metallurgical Transactions A, 1982, 13: 135−140.

[22] FURUHARA T, MAKI T, MAKINO T. Microstructure control by thermomechanical processing in β-Ti−15−3 alloy [J]. Journal of Materials Processing Technology, 2001, 117(3): 318−323.

[23] MAO Qing-zhong, ZHANG Yu-sheng, LIU Ji-zi, ZHAO Yong-hao. Breaking material property trade-offs via macrodesign of microstructure [J]. Nano Letters, 2021, 21(7): 3191−3197.

[24] WILLIAMSON G K, HALL W H. X-ray line broadening from filed aluminium and wolfram [J]. Acta Metallurgica, 1953, 1(1): 22−31.

[25] TAKEBAYASHI S, KUNIEDA T, YOSHINAGA N, USHIODA K, OGATA S. Comparison of the dislocation density in martensitic steels evaluated by some X-ray diffraction methods [J]. ISIJ International, 2010, 50(6): 875−882.

[26] KASCHEL F R, VIJAYARAGHAVAN R K, SHMELIOV A, MCCARTHY E K, CANAVAN M, MCNALLY P J, DOWLING D P, NICOLOSI V, CELIKIN M. Mechanism of stress relaxation and phase transformation in additively manufactured Ti−6Al−4V via in situ high temperature XRD and TEM analyses [J]. Acta Materialia, 2020, 188: 720−732.

[27] PANTAWANE M V, DASARI S, MANTRI S A, BANERJEE R, DAHOTRE N B. Rapid thermokinetics driven nanoscale vanadium clustering within martensite laths in laser powder bed fused additively manufactured Ti6Al4V [J]. Materials Research Letters, 2020, 8(10): 383−389.

[28] ZHANG Chong-le, BAO Xiang-yun, HAO Meng-yuan, CHEN Wei, ZHANG Dong-dong, WANG Dong, ZHANG Jin-yu, LIU Gang, SUN Jun. Hierarchical nano-martensite-engineered a low-cost ultra-strong and ductile titanium alloy [J]. Nature Communications, 2022, 13(1): 5966.

[29] KOCKS U.F, MECKING H. Physics and phenomenology of strain hardening: The FCC case [J]. Progress in Materials Science, 2003, 48: 171−273.

[30] BAHADOR A, UMEDA J, YAMANOGLU R, AMRIN A, ALHAZAA A, KONDOH K. Ultrafine-grain formation and improved mechanical properties of novel extruded Ti−Fe−W alloys with complete solid solution of tungsten [J]. Journal of Alloys and Compounds, 2021, 875: 160031.

[31] de FORMANOIR C, MARTIN G, PRIMA F, ALLAIN S Y. P, DESSOLIER T, SUN Fan, VIVÈS S, HARY B, BRÉCHET Y, GODET S. Micromechanical behavior and thermal stability of a dual-phase $\alpha+\alpha'$ titanium alloy produced by additive manufacturing [J]. Acta Materialia, 2019, 162: 149−162.

[32] CHEN Cai, HAN Dong-sheng, SONG Yu-tao, WANG Ming-chuan, LI Yu-sheng, XU Shun, YANG Sen, LIU Ji-zi. Effect of grain size and temperature on deformation mechanism of commercially pure titanium [J]. Transactions of Nonferrous Metals Society of China, 2023, 33(11): 3332−3347.

[33] FAN Lei, YANG Tao, ZHAO Yi-lu, LUAN Jun-hua, ZHOU Gang, WANG Hao, JIAO Zeng-bao, LIU C T. Ultrahigh strength and ductility in newly developed materials with coherent nanolamellar architectures [J]. Nature Communications, 2020, 11(1): 6240.

[34] RUSSELL K C, BROWN L M. A dispersion strengthening model based on differing elastic moduli applied to the iron−copper system [J]. Acta Metallurgica, 1972, 20(7): 969−974.

[35] YANG M X, YUAN F P, XIE Q G, WANG Y D, MA E, WU X L. Strain hardening in Fe−16Mn−10Al−0.86C−5Ni high specific strength steel [J]. Acta Materialia, 2016, 109: 213−222.

[36] SU Jin-long, JI Xian-kun, LIU Jin, TENG Jie, JIANG Fu-lin, FU Ding-fang, ZHANG Hui. Revealing the decomposition mechanisms of dislocations and metastable α' phase and their effects on mechanical properties in a Ti−6Al−4V alloy [J]. Journal of Materials Science & Technology, 2022, 107: 136−148.

[37] BARRIOBERO-VILA P, VALLEJOS J M, GUSSONE J, HAUBRICH J, KELM K, STARK A, SCHELL N, REQUENA G. Interface-mediated twinning-induced plasticity in a fine hexagonal microstructure generated by additive manufacturing [J]. Advanced Materials, 2021, 33(52): e2105096.

[38] LUO Hao, LI Yu, LI Wei, ZHONG Shao-xiong, XU Chun, JIA Xiao-shuai. Interactions of nanoprecipitates, metastable austenite, and Lüders banding in an ultra-low carbon medium Mn steel with abnormal strength dependence of hydrogen embrittlement [J]. Materialia, 2022, 22: 101380.

[39] AYAS C, DESHPANDE V S, FLECK N A. A fracture criterion for the notch strength of high strength steels in the presence of hydrogen [J]. Journal of the Mechanics and Physics of Solids, 2014, 63: 80−93.

[40] OUDRISS A, CREUS J, BOUHATTATE J, CONFORTO E, BERZIOU C, SAVALL C, FEAUGAS X. Grain size and grain-boundary effects on diffusion and trapping of hydrogen in pure nickel [J]. Acta Materialia, 2012, 60(19): 6814−6828.

[41] ZHOU Xiao, MOUSSEAU N, SONG Jun. Is hydrogen diffusion along grain boundaries fast or slow? Atomistic origin and mechanistic modeling [J]. Physical Review Letters, 2019, 122(21): 215501.

[42] DADFARNIA M, MARTIN M L, NAGAO A, SOFRONIS P, ROBERTSON I M. Modeling hydrogen transport by dislocations [J]. Journal of the Mechanics and Physics of Solids, 2015, 78: 511−525.

[43] YUAN Shu-lin, ZHU Ya-xin, ZHAO Lv, LIANG Shuang, HUANG Min-sheng, LI Zhen-huan. Key role of plastic strain gradient in hydrogen transport in polycrystalline materials [J]. International Journal of Plasticity, 2022, 158: 103409.

[44] KONG De-cheng, ZHAO De-chao, ZHU Guo-liang, NI Xiao-qing, ZHANG Liang, WU Wen-heng, MAN Cheng, ZHOU Yi-qi, DONG Chao-fang, SUN Bao-de. Heat treatment effects on the hydrogen embrittlement of Ti6Al4V fabricated by laser beam powder bed fusion [J]. Additive Manufacturing, 2022, 50: 102580.

[45] YUE Fang-ya, LI Yu-hao, ZHOU Hong-bo, ZHANG Ying, LU Guang-hong. Insight into the enhancement effect of rhenium-rich precipitation on hydrogen retention in

tungsten by investigating the behaviors of hydrogen in tungsten−rhenium sigma phase [J]. International Journal of Hydrogen Energy, 2019, 44(45): 24880−24894.

[46] LUO Hong, ZHAO Bo, PAN Zhi-min, FU Yu, LI Xiao-gang. Hydrogen induced microstructure evolution and cracking mechanism in a metastable dual-phase high-entropy alloy [J]. Materials Science and Engineering: A, 2021, 819: 141490.

[47] NOVAK P, YUAN R, SOMERDAY B P, SOFRONIS P, RITCHIE R O. A statistical, physical-based, micro-mechanical model of hydrogen-induced intergranular fracture in steel [J]. Journal of the Mechanics and Physics of Solids, 2010, 58(2): 206−226.

[48] SETOYAMA D, MATSUNAGA J, MUTA H, UNO M, YAMANAKA S. Mechanical properties of titanium hydride [J]. Journal of Alloys and Compounds, 2004, 381: 215−220.

[49] SHIH D S, ROBERTSON I M, BIRNBAUM H K. Hydrogen embrittlement of α titanium: In situ TEM studies [J]. Acta Metallurgica, 1988, 36(1): 111−124.

[50] WU Wang-ping, HE Guang, HUANG Jia-qi, ZHANG Ao, LIU Xi-liang, OUYANG Zhong, SUN Zi-long, GUAN Li, CHU Song, LI Peng, JIANG Peng, ZHANG Yi. Influence of electrochemically charged hydrogen on mechanical properties of Ti−6Al−4V alloy additively manufactured by laser powder-bed fusion (L-PBF) process [J]. Materials Science and Engineering: A, 2023, 866: 144339.

[51] NGUYEN T D, SINGH C, LEE D H, KIM Y S, LEE T, LEE S Y. Deciphering hydrogen embrittlement mechanisms in Ti6Al4V alloy: Role of solute hydrogen and hydride phase [J]. Materials (Basel), 2024, 17(5): 1178.

[52] ZHANG Hong-liang, HOU Jia-ping, ZHANG Da-zheng, LI Wei-juan, XU Jia-kai, PANG Qi-hang, ZHU Qing-yan, ZHANG Jun-kai. Effect of quenching, lamellarizing, and tempering on reversed austenite and cryogenic toughness of 9Ni steels [J]. Journal of Materials Engineering and Performance, 2024, 33(5): 2349−2357.

通过可逆相变改善激光粉末床熔融 Ti−6Al−4V 合金的延展性和抗氢脆性

马焕祺[1]，黎 雨[1,2]，李 伟[2]，徐 春[1]

1. 上海应用技术大学 材料科学与工程学院，上海 201408；
2. 上海交通大学 材料科学与工程学院，上海 200240

摘 要：为了同时提高 Ti−6Al−4V 合金的强度−塑性协同和抗氢脆性，对激光粉末床熔融的合金进行后退火处理以引入可逆相变。通过电子背散射衍射、透射电子显微镜、慢应变速率拉伸、氢渗透和热脱附谱等测试手段分析了合金的显微组织、力学性能和氢脆行为。初始打印样品虽然强度高，但伸长率低且氢脆敏感性高。在 550 ℃退火后，伸长率显著提高，但氢扩散速率同时增加，促进了脆性氢化物的形成。在 750 ℃退火后，通过 $\alpha'\rightarrow\beta\rightarrow\alpha'$ 可逆相变形成了 $\alpha'/\beta/\alpha'$三明治层状结构，在保持高强度(~1116 MPa)的同时提高了抗氢脆性(总伸长率损失降至 12%)。纳米 β 相的引入和软取向的 α'晶粒显著抑制了氢化物的形成和氢致裂纹的扩展。

关键词：Ti−6Al−4V 合金；氢脆；强度−塑性协同；后退火；可逆相变

(Edited by Wei-ping CHEN)